

HUMBI 1.0: HUman Multiview Behavioral Imaging Dataset

*Zhixuan Yu[†] *Jae Shin Yoon[†] Prashanth Venkatesh[†] Jaesik Park[‡] Jihun Yu[#] Hyun Soo Park[†]
[†]University of Minnesota [‡]Intel [#]BinaryVR

{yu000064, jsyoon, venka220, hspark}@umn.edu, jaesik.park@intel.com, jihun.yu@binaryvr.com



Figure 1: We present HUMBI dataset—human behavioral imaging using a large scale multi-camera system composed of 107 cameras (164 distinctive subjects). We generate computational models for 5 elementary body signals: face, gaze, hand, body, and cloth. The computational models are overlaid with the multiview images.

Abstract

This paper presents a new dataset called HUMBI — a large corpus of high fidelity models of behavioral signals in 3D from a diverse population measured by a massive multi-camera system. With our novel design of a portable imaging system (consists of 107 HD cameras), we collect human behaviors from 164 subjects across gender, ethnicity, age, and physical condition at a public venue. Using the multi-view image streams, we reconstruct high fidelity models of five elementary parts: gaze, face, hands, body, and cloth.

As a byproduct, the 3D model provides geometrically consistent image annotation via 2D projection, e.g., body part segmentation. This dataset is a significant departure from the existing human datasets that suffers from subject diversity. We hope the HUMBI opens up a new opportunity for the development for behavioral imaging.

1. Introduction

We are witnessing a revolution of computer vision systems that changes the our conception and use of large-scale data. Realtime object recognition, virtual telepresence, and

*Both authors contributed equally to this work

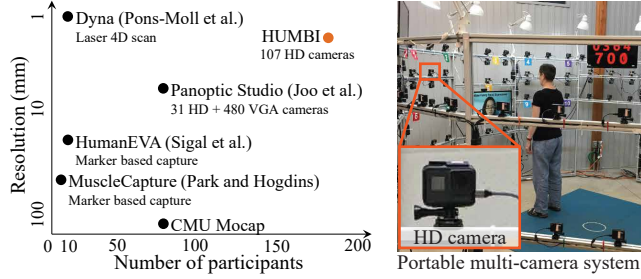


Figure 2: The requirements of measurement precision (resolution) and subject diversity (number of participants) conflict with each other, which limits the model expressibility of the existing datasets. We present the HUMBI dataset that achieves both precision and diversity by leveraging a portable multi-camera system (107 HD cameras) deployed at a public venue.

autonomous driving are directly or indirectly intertwined with our lives, and they (and other vision systems) will certainly permeate society more. However, such vision systems still cannot observe and process underlying mental states such as intent, emotion, and attention while nearly any three-year-old can effortlessly *read* the meaning of a simple nod, eye contact, or a pointed finger. What makes the three-year-old — and the rest of us — so different from these vision systems? We conjecture that the ability to discern the behaviors/social signals [2] such as gaze direction, facial expression, and body gesture is key.

Our behavioral signals are subtle and highly person-specific [50]. To make sense of such signals, two requirements must be met: (1) precise measurements of natural behaviors at millimeter and millisecond scale; and (2) a large collection of the behaviors from diverse individuals across gender, ethnicity, age, and physical condition. In practice, however, precision and diversity conflict with each other. Precise measurements need a specialized equipment such as a 4D scanner or a dense set of cameras [3–5, 16, 21, 28, 37, 53, 54], which precludes from voluntary participations from a large and diverse pool of subjects, i.e., the subject recruitment mostly relies on invitation. For example, most existing datasets of human body motion are composed of a number of scripted performances by a few actor/actress [1, 20, 21, 28, 41]. Fig. 2 (left) illustrates this conflicting nature (resolution vs. number of participants) of the state-of-the-art datasets, which fundamentally limits the computational characterization of the behavioral signals.

In this paper, we present the *HUMBI* (HUMAN Multiview Behavioral Imaging) dataset — a new corpus of high fidelity reconstruction of natural behavioral signals in 3D from a diverse population measured by a large-scale multi-camera system. To address aforementioned challenges, we have designed a novel *portable* multi-camera system composed of 107 HD synchronized cameras (up to 10ms) as shown in Fig. 2 (right). It is the first portable system capa-

ble of capturing total body with full range of motion (up to two subjects) from various locations. Notably, we deployed the system at the State Fair that attracts more than two millions of attendees annually. This public deployment allows capturing multiview visual data from a diverse population, which constitutes 164 independent subjects.

With these multiview image streams, we reconstruct high fidelity 3D models for the five elementary body signals. (1) Gaze: we reconstruct the 3D gaze direction towards the point of regard (eye-in-head motion) given the 3D face pose from a gaze calibration procedure; (2) Facial expression: we leverage multiview images to recover the face geometry, appearance, and reflectance using a 3D morphable model [6]; (3) Hands: we exploit the hand pose recognition from the multiview images to triangulated 3D hand configuration and fit to an in-house hand mesh model; (4) Body: a 3D parametric model [28] is reconstructed by aligning with the body volumetric reconstruction (using shape-from-silhouette) with body part segmentation; (5) Cloth: the geometry of the garment is modeled by a 3D CAD cloth model. As a byproduct, these reconstructed 3D models automatically produce geometrically consistent annotations for body semantic segmentation, gaze/pose, view-dependent appearance, and reflectance.

The main properties of HUMBI is: (1) complete: it captures total body including gaze, face, finger, foot, body, and cloth, which is critical for modeling reciprocal behavioral signals, e.g., a synchrony between face and hand movements; (2) dense: 107 HD cameras (70 body cameras and 35 face/gaze cameras) create a dense light field that can observe the detailed behavioral signals with minimal self-occlusion. Also the dense light field provides the variation of appearance with respect to the viewpoint changes [27]; (3) natural: the subjects are all voluntary participants (not an actor/actress) where their behaviors are naturally induced by the demonstrative video, which creates a number of person-specific movements; (4) diverse: each subject has unique physical appearance with natural clothing; (5) fine: the high fidelity 3D model reconstructed running at high framerate can model the fine-grained behavioral signals at millimeter and millisecond scale.

To our best knowledge, this is the first dataset that includes a diverse population measured by a massive multi-camera system. The core contributions include: (a) the unique design of the portable multi-camera system that can be deployed at various venues to capture diverse subjects; (b) the terascale multiview visual data that measure the detailed human behaviors at millimeter scale; (c) the high fidelity model for gaze, face, hands, body, and cloth, and their reconstruction algorithm; and (d) geometrically consistent multiview image annotations via 2D projection of 3D models. The HUMBI will open up a new opportunity to develop computer vision systems that can precisely decode

the minute details of our behaviors in daily living space, which will truly facilitate smart home/hospital that assists millions of the elderly, children, and patients.

2. Related Work

Humans transmit and respond to many different behavioral signals such as gaze movement, facial expression, and body gestures when they interact with others [35, 50]. Effective signaling and interpretation of signals are the basis of successful social performance, for example, in business [10, 11, 33]. Researchers have developed various computational models to measure, model, and predict the behavioral signals [14, 34]. Some behavioral signals such as hand-flapping, repeating sounds, and deficits of joint attention have shown to be early markers of the autistic spectrum disorder, and computational tools have been designed to detect these symptoms [30, 38]. The data of behavioral signals is the key enabling factor, which builds computational models. Here, we briefly review the existing datasets for gaze, face, hand, body, and cloth. These datasets are summarized in Table 1.

Gaze Sigal *et al.* [41] proposed a passive, appearance-based approach that focus on gaze locking instead of gaze tracking, which can sense eye contact in an image. Sugano *et al.* [45] proposed a method for reconstructing gaze from low-resolution eye images. Unlike many other methods which assume person-specific training data, a large amount of cross-subject training data was created and used to train a 3D gaze estimator. Mora *et al.* [29] introduced a novel database along with a common framework for the training and evaluation of gaze estimation approaches. To drive the work on appearance-based gaze estimation, Zhang *et al.* [56] presented the MPII-Gaze dataset that collected gazes in the wild.

Face During last decades, quite a few face datasets and models have been created to accelerate research in this area. To address the short comings of CMU PIE data [42] in limited number of subjects, recording session and expression types, CMU Multi-PIE dataset [17] came out, which captures more than 300 hundreds people displaying diverse expressions under 15 view points and 19 illumination conditions. The development of face datasets drove the development of face models like 3DMM [6], the method described in which recognize faces across variations in pose and illuminations, including cast shadows and specular reflections. Another generative face model proposed by Basel *et al.* [32] facilitates invariant face recognition across sensors by separating pose, lighting, imaging and identity parameters. Recently, a large-scale 3D Morphable Models LSM was constructed [7]. It contains nearly 10K distinct facial identities and achieved state-of-art results according to qualitative and quantitative evaluations by that time.

Hand Dexterous hand manipulation through behavioral sig-

naling frequently introduces severe self-occlusion, which is the main challenge of recovering 3D finger configuration. A depth image that provides trivial hand segmentation in conjunction with tracking has been used to establish the ground truth hand pose [46–49]. However, as the occlusion still play a key role, these datasets involve with large manual adjustments, which limits the size of data. This has been addressed by using magnetic sensors on hands that can precisely measure the joint angle, which allows automatically computing the 3D hand pose using forward kinematics [51, 55]. Notably, a multi-camera system has been used to annotate the hand using 3D bootstrapping [43], which can provide the hand annotations for the RGB data.

Body Unlike human face, the body has a complex geometry and dynamics. To model such motion complexity, 3D optical motion capture systems have been used to model free ranging activities [1, 18]. The motion capture system produces accurate reconstruction (at submillimeter scale) while the resolution (density) of measures are rather sparse, e.g., one per limb. Densification of the markers induces a large data association problem, which has been addressed by leveraging the spatiotemporal structure of the markers [31]. Markerless motion capture is a viable solution for densification of body capture. Multi-camera systems (markerless) have been used to capture a diverse set of body poses while a few actors and actresses performing a few scripted activities such as drinking, answering cellphone, and sitting [20, 41]. Further, a 4D scanner [37] enables extreme quality body capture, which allows building a parametric human models, e.g., SMPL [28]. Another notable body datasets rely on the manual annotation of image-to-surface correspondences on 50K COCO images [26]. However, the human manual annotations are often erroneous.

Cloth For simulation purpose, many previous works have proposed to capture the natural property of cloth affected by human body using 3D segmentation on the scanned human in cloth using 4D scanner [36] or multiple synchronized cameras [8, 52]. However, their methods does not ensure the same topology across the time which is key component of recent learning approaches, and the diversity of pose and shape in cloth is limited to propose the dataset. To the best of our knowledge, this is the first attempts to propose public 3D cloth dataset with its associated 2D image pair captured under the natural human performance. Our method is not based on 3D segmentation but based on fitting expert designed cloth templates to the 3D reconstruction scanned by multiview system.

3. Portable Behavioral Imaging System

We design a unique *portable* multi-camera system that was deployed in the State Fair to capture the human behavioral signals from a diverse population. 164 subjects (Fig. 3)

| Dataset | # of subjects | Measurement method | Gaze | Face | Hand | Body | Cloth |
|--------------------------|--------------------|--|----------|------|------|------|----------------|
| Columbia gaze [44] | 56 | 5 cameras | ✓(fixed) | | | | |
| UT multiview gaze [45] | 50 | 8 cameras | ✓(fixed) | | | | |
| Eyediap [29] | 16 | 1 depth camera and 1 HD camera | ✓(free) | | | | |
| MPII gaze [56] | 15 | 1 camera | ✓(free) | | | | |
| CMU Multi-PIE [17] | 337 | 15 cameras | ✓ | | | | |
| 3DMM [6] | 200 | 3D scanner | ✓ | | | | |
| BFM [32] | 200 | 3D scanner | ✓ | | | | |
| ICL [7] | 10,000 | 3D scanner | ✓ | | | | |
| NYU Hand [49] | N/A (81K samples) | Depth camera | | ✓ | | | |
| HandNet [51] | N/A (213K samples) | Depth camera and magnetic sensor | | ✓ | | | |
| BigHand 2.2M [55] | N/A (2.2M samples) | Depth camera and magnetic sensor | | ✓ | | | |
| CMU Mocap [1] | ~100 | Marker-based | | | | ✓ | |
| CMU Skin Mocap [31] | <10 | Marker-based | | | | ✓ | |
| INRIA [23] | N/A | Markerless (34 cameras) | | | | ✓ | |
| Human EVA [41] | 4 | Marker-based and Markerless (4-7 cameras) | | | | ✓ | ✓(natural) |
| Human 3.6M [20] | 11 | Markerless (depth camera and 4 HD cameras) | | | | ✓ | |
| Panoptic Studio [21, 43] | ~100 | Markerless (31 HD and 480 VGA cameras) | | | | ✓ | |
| 4D scan [37] | 10 | Markerless (22 pairs of stereo cameras) | | | | ✓ | |
| 4D cloth scan [36] | 10 | Markerless (22 pairs of stereo cameras) | | | | ✓ | ✓(synthesized) |
| HUMBI | 160 (185M images) | Markerless (107 HD cameras) | ✓(free) | ✓ | ✓ | ✓ | ✓(natural) |

Table 1: Comparison of HUMBI to other behavioral signal datasets



Figure 3: Example of subjects. 164 subjects across diverse gender, ethnicity, age were captured by our behavioral imaging system.

voluntarily participated¹ in the behavioral imaging in Labor Day 2018 (9 hours). The cameras continuously recorded the performance at 60Hz, which constitutes nearly 185 million images (\sim 14TB).

Hardware The capture system is built upon re-configurable a dodecagon frame with 3.5 m diameter and 2.5 m height using T-slot structural framing (80/20 Inc.). It is composed of 107 GoPro HD cameras (HERO 6 BLACK Edition), one LED display for an instructional video, four LED displays for video synchronization, and 12 white light lamps for illumination. Among 107 cameras, 69 cameras were uniformly placed along the two levels of the dodecagon arc (0.8 m and 1.6 m) for body and cloth capture, and 38 cameras were placed over the frontal hemisphere for face and gaze capture as shown in Fig. 2. 9 hours of videos are recorded in the local micro HD card (128GB) in each camera.

Performance Instructional Video To guide the behavioral signals, we created four performance instructional videos

(2 minutes) that demonstrate the intended actions. Each video is composed of four actions: (1) to find and look at the requested number tag posted on the camera stage; (2) to follow 20 distinctive dynamic facial expressions (e.g., eye rolling, frowning, and jaw opening); (3) to follow range of motion, which allows them to move their full body, (4) to follow slow and full speed dance performances curated by a professional choreographer.

Synchronization and Calibration We use the four LED screens to display 1KHz timestamp to synchronize cameras. Given the series of timestamps of a reference camera, we compute the coarse offset of the rest and refine it with OCR (tesseract) and further with manual verification and adjustment. This synchronization results in at most 7ms offset between cameras. Camera intrinsic and extrinsic parameters are calibrated by standard structure from motion using COLMAP software [40]. All images are extracted and undistorted using a fisheye lens model [12].

¹Each subject filled a consent form of data release before the capture.



Figure 4: A example of synchronized image frames at a certain time stamp. 107 GoPro HD cameras captures diverse viewpoints of the subject and facial expressions simultaneously.

4. Computational Behavioral Representation

Given the synchronized and massive multiview image streams, we reconstruct behavioral signals for each subject in 3D. In particular, we focus on five elementary body signals: gaze, face, finger, body, and cloth. We use 3D body keypoint reconstruction to compute the base human skeleton and generate a high fidelity mesh model by fitting to multiview images. Note that each time instant is processed independently, i.e., no temporal filtering or regularization has been applied.

4.1. 3D Keypoint Reconstruction

Given a set of synchronized multiview images, we compute 3D body landmark locations including face, body joint (including feet), and finger joint using a pose detector [9]. We detect the poses of multiple persons in each image and identify the same person via a geometric verification across multiview images where the 3D location of each joint can be triangulated with RANSAC [15] and followed by the non-linear refinement by minimizing reprojection error [19].

4.2. Gaze

We represent the gaze direction with respect to a moving coordinate system defined the head orientation computed by facial keypoints as shown in Fig. 5. The origin of the coordinate system is the center of eyes, $\mathbf{o} = (\mathbf{p}_l + \mathbf{p}_r)/2$ where $\mathbf{p}_l, \mathbf{p}_r \in \mathbb{R}^3$ are the locations of the left and right eyes; the x -axis is the direction along the line joining the two eyes, $\mathbf{a}_x = (\mathbf{p}_l - \mathbf{p}_r)/\|\mathbf{p}_l - \mathbf{p}_r\|$; the z -axis is the direction pointing forward and perpendicular to $(\mathbf{p}_l, \mathbf{p}_r, \mathbf{p}_c)$ plane, where \mathbf{p}_c is the location of chin point, i.e. $\mathbf{a}_z = (\mathbf{p}_c - \mathbf{o}) \times \mathbf{a}_x / \|(\mathbf{p}_c - \mathbf{o}) \times \mathbf{a}_x\|$; y -axis is $\mathbf{a}_z \times \mathbf{a}_x$.

The gaze direction is a unit vector $\mathbf{g} = \mathbf{R}^{\text{head}}(\mathbf{m} - \mathbf{o})/\|\mathbf{m} - \mathbf{o}\|$, where $\mathbf{m} \in \mathbb{R}^3$ is the location for the point of regard (the numbered tag marker), and $\mathbf{R}^{\text{head}} = [\mathbf{a}_x^T \ \mathbf{a}_y^T \ \mathbf{a}_z^T]^T \in SO(3)$ is the rotation that transforms from the world coordinate system to the head.

Using the head coordinate system, we make a 3D cylind-

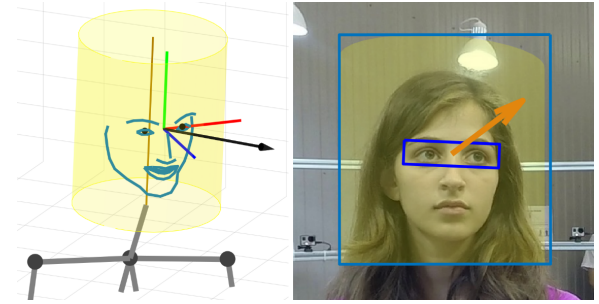


Figure 5: Gaze signals computed by our system (Sec. 4.2). (Left) 3D demonstration of captured gaze placed on the black dotted body joints. Black arrow is gaze direction. Red, green and blue segment are x , y and z -axis of gaze frame. Brown segment is the center axis of the head cylinder. (Right) Gaze overlaid on a color image. Orange arrow is gaze direction. Dark blue box indicates eye region. Blue box wraps face. Yellow area is projection of the cylinder.

der to define the face region. The center of cylinder is defined to be the midpoint between leftmost and rightmost facial contour points. Orientation of cylinder is defined to be same as y -axis of the head coordinate system. Radius and height of cylinder is determined to fully cover face keypoints. With this 3D cylinder, it is able to determine a rectangular bounding box in the image domain. The bounding box is rectified in the sense that the center axis of the cylinder coordinate become upright. We also define bounding box for eyes area by using projection of two eye keypoints. We use this 3D cylindrical representation to crop the region of face and gaze from multiview images.

4.3. Face

We reconstruct a high fidelity face model using multiview images by minimizing the following cost:

$$E^{face} = E_k^{face} + \lambda_a^{face} E_a^{face}, \quad (1)$$

where E_k^{face} and E_a^{face} are errors of 3D keypoint and appearance, respectively.

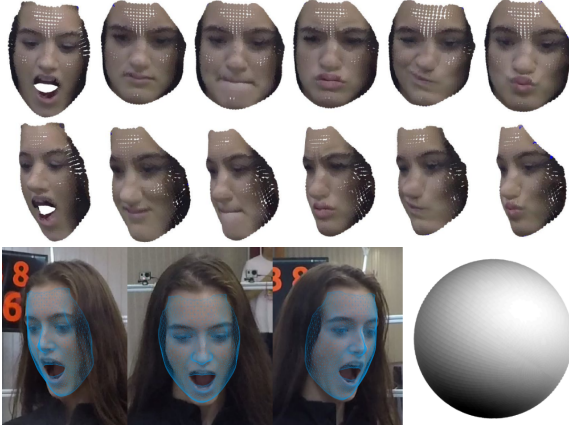


Figure 6: Face reconstruction (Sec. 4.3). (Top) Recovered 3D faces with various expressions (Bottom left) Alignment between projected mesh and subject’s face. (Bottom right) Estimated illumination condition.

Shape and Expression We represent a 3D face using a high resolution blended shape model [6, 7]:

$$\mathbf{S}(\boldsymbol{\alpha}^s, \boldsymbol{\alpha}^e) = \mathbf{S}_0 + \sum_{i=1}^{K_s} \alpha_i^s \mathbf{S}_i + \sum_{i=1}^{K_e} \alpha_i^e \mathbf{E}_i, \quad (2)$$

where $\mathbf{S} \in \mathbb{R}^{3 \times D_s}$ is the 3D face, \mathbf{S}_0 is the meanface, \mathbf{S}_i and α_i^s are the i^{th} shape basis and its coefficient, and \mathbf{E}_i and α_i^e are the i^{th} expression basis and its coefficient. D_s is the number of points in the shape model.

We align this 3D face model with the 3D reconstructed facial keypoints:

$$E_k^{face}(s, \mathbf{T}, \boldsymbol{\alpha}^s, \boldsymbol{\alpha}^e) = \sum_i^{D_k} \|\mathcal{K}^f(i) - (s\mathbf{T}(\mathcal{N}_i(\mathbf{S})))\|^2$$

where $\mathcal{K}^f = \{\mathbf{k}_i\}_{i=1}^{D_k}$, $\mathcal{K}^f(i)$ is i^{th} facial keypoints, and \mathcal{N} returns a point in shape \mathbf{S} corresponding to the keypoints. D_k is the number of facial keypoints. s and \mathbf{T} are the parameters for a similarity transformation (scale, rotation + translation respectively).

Appearance We represent the 3D face texture with linear model:

$$\mathbf{F} = \mathbf{F}_0 + \sum_{i=1}^{K_f} \alpha_i^f \mathbf{F}_i, \quad (3)$$

where $\mathbf{F} \in \mathbb{R}^{3 \times D_s}$ is the 3D face texture, \mathbf{F}_0 is the mean texture model, \mathbf{F}_i and α_i^f are the i^{th} texture basis and its coefficient.

The appearance model is combination of texture and illumination: $\mathbf{A} = \mathcal{I}(\mathbf{F}, \mathbf{S}, \boldsymbol{\alpha}^h)$ where \mathbf{A} is the RGB color for a 3D face and \mathcal{I} uses Lambertian illumination to estimate the appearance. We model the illumination using the

spherical harmonics basis model where $\boldsymbol{\alpha}^h$ is the coefficient for the harmonics. From this, the error of appearance is:

$$E_a^{face}(\boldsymbol{\alpha}^s, \boldsymbol{\alpha}^e, \boldsymbol{\alpha}^f, \boldsymbol{\alpha}^h) = \sum_j \|\mathbf{a}_j - \phi_j(\mathbf{A})\|^2, \quad (4)$$

where $\phi_j(\mathbf{A})$ is the projection of the appearance \mathbf{A} onto the j^{th} camera, and \mathbf{a}_j is the face appearance in the j^{th} image.

We optimize Eq. (1) using a nonlinear least squares solver with ambient light initialization. Fig. 6 illustrate the resulting face reconstruction where we compute the shape, expression, texture and reflectance.

4.4. Body

We recover a parametric 3D body model [28] using multiview images initialized by volume reconstruction.

4.4.1 Volume Reconstruction

We leverage shape-from-silhouette² [24] to compute a coarse estimate of the body volume. The foreground masks are computed using human body segmentation [25] over the multiview images, which provides reliable volumetric reconstruction [54]. A surface having vertices $\mathcal{V} = \{\mathbf{v}_i\}_{i=1}^n$, where $\mathbf{v} \in \mathbb{R}^3$, is recovered from valid voxels using Poisson surface reconstruction [22] as shown in Fig. 7.

4.4.2 SMPL Fitting

With 3D body keypoints \mathcal{K} (Sec. 4.1) and volume \mathcal{V} (Sec. 4.4.1), SMPL body template [28] $\mathcal{M}^t = \{\mathbf{m}_i\}_{i=1}^{6890}$, where $\mathbf{m}_i \in \mathbb{R}^3$, is aligned with \mathcal{K} and \mathcal{V} for the body shape.

A SMPL body model \mathcal{M} is represented by a function $\mathcal{F}(\mathcal{M}^t; \boldsymbol{\theta}, \boldsymbol{\beta}, \mathbf{t}, s)$ that deforms a template model \mathcal{M}^t using linear blend skinning (LBS) function with trained pose and gender dependent blending weights. $\boldsymbol{\beta} \in \mathbb{R}^{10}$ is for linear shape basis trained with a thousand of human body scans, $\boldsymbol{\theta} = \{\boldsymbol{\theta}_i\}_{i=1}^{23}$, where $\boldsymbol{\theta} \in \mathbb{R}^3$, is defined as Euler angles for 23 body joints (one root joint and 22 relative joints between body parts), and $\mathbf{t} \in \mathbb{R}^3$ and $s \in \mathbb{R}$ denote the translation and scale factor. The relative coordinates for body joints $\mathcal{J}(\boldsymbol{\beta}, \boldsymbol{\theta}) = \{\mathbf{j}_i\}_{i=1}^{23}$, where $\mathbf{j} \in \mathbb{R}^3$, are calculated by traversing the relative rotation $\boldsymbol{\theta}_{i \in [2, 23]}$ from their parent joint, where only root joint $\boldsymbol{\theta}_1$ is associated with global rotation, and its corresponding rotation matrix is denoted as $\mathbf{R}^{root} \in SO(3)$.

We estimate the optimal parameters for SMPL model by minimizing the following objective function:

$$E^{body}(\boldsymbol{\theta}, \boldsymbol{\beta}, \mathbf{t}, s) = E_p^{body} + \lambda_s^b E_s^{body} + \lambda_r^b E_r^{body}, \quad (5)$$

where E_p^{body} , E_s^{body} , and E_r^{body} are errors for body pose, shape, and shape prior, and λ_s^b and λ_r^b control their importance.

²Multiview stereo [40] is complementary to the volume reconstruction.



Figure 7: Body and cloth reconstruction. (From left to middle) 3D Body joint \mathcal{K} is computed from images (Sec. 4.1). Volume of a subject \mathcal{V} is obtained (Sec. 4.4.1). Estimated SMPL body model \mathcal{M} (Sec. 4.4.2). Cloth templates consist of dense mesh $\mathcal{C}^{t,b}$ and annotated keypoints $\mathcal{K}^{t,b}$ are prepared. The cloth has label map $\mathcal{L}^{t,b}$ for part adaptive alignment (Sec. 4.5). (Right) Three steps for cloth fitting (Sec. 4.5). (1) Template cloth \mathcal{C}^t and \mathcal{C}^b are roughly aligned to estimated body joint \mathcal{K} . (2) \mathcal{C} and body model \mathcal{M} are densely aligned and produce $\tilde{\mathcal{C}}$. (3) $\tilde{\mathcal{C}}$ is aligned with the body volume \mathcal{V} .

Pose E_p^{body} penalizes the distance between reconstructed 3D body joints \mathcal{K} and the SMPL model joints \mathcal{J} :

$$E_p^{body}(\Theta, \beta; \mathcal{K}, \mathcal{J}) = \sum_i^{18} \|\mathcal{K}(i) - \mathcal{J}(\mathcal{E}(i))\|^2, \quad (6)$$

where $\mathcal{K}(i)$ is the i^{th} keypoints in \mathcal{K} , and $\mathcal{E}(\cdot)$ returns its corresponding joint index on \mathcal{J} . Notably, we map the keypoint [9] joints to the topologically closest joints in SMPL to account a discrepancy on joint descriptions.

Shape E_s^{body} encourages the shape of SMPL body model to be aligned to the volume of body \mathcal{V} (Sec. 4.4.1) by establishing correspondence based on iterative closest point (ICP) [39]:

$$E_s^{body}(\Theta, \beta; \mathcal{V}, \mathcal{M}) = \sum_{\mathbf{v} \in \mathcal{V}} \|\mathbf{v} - \mathcal{M}(\tau(\mathbf{v}, \mathcal{M}))\|^2, \quad \text{where } \tau(\mathbf{v}, \mathcal{M}) = \operatorname{argmin}_i \|\mathbf{v} - \mathcal{M}(i)\|^2, \quad (7)$$

$\mathcal{M}(i)$ is a i^{th} element of \mathcal{M} , and $\tau(\cdot)$ returns an index of the closest point.

Shape Prior E_r^{body} penalizes the difference between estimated shape β and the subject-aware mean shape β^{prior} as follows:

$$E_r^{body}(\beta; \beta^{prior}) = \|\beta - \beta^{prior}\|^2. \quad (8)$$

This prevents unrealistic shape fitting due to the estimation noise/error, e.g., long hair covering body. To obtain the shape prior β^{prior} , we solve the Eq. (5) without E_r^{body} using the recovered volumes of the same subject and take the median β for robustness.

4.5. Cloth

We represent the cloth with an expert-crafted cloth template as $\mathcal{C} = \{\mathbf{c}_i\}_{i=1}^{N_c}$, where $\mathbf{c} \in \mathbb{R}^3$, based on the assumption of minimally clothed shape [36]. This template has

cloth joint \mathcal{K}^c which is defined by manual annotation to be similar to \mathcal{K} as shown in Fig. 7. We regard a cloth consists of top \mathcal{C}^t and bottom \mathcal{C}^b .

The key idea of cloth fitting is to fit $\mathcal{K}^{t/b}$ to estimated body model joint \mathcal{K} , and then align \mathcal{C} and \mathcal{M} to make a cloth template tightly aligned to the SMPL body model. The next step refines the cloth to be aligned with the body volume \mathcal{V} . Instead of directly aligning \mathcal{C} to \mathcal{V} , we observe this approach is more structured and produces stable results. This procedure is shown in Fig. 7.

To align \mathcal{C} with \mathcal{M} , we compute the local deformation field $\tilde{\mathcal{D}} = \{\tilde{\mathbf{R}}_i \in SO(3), \tilde{\mathbf{t}}_i \in \mathbb{R}^3\}_{i=1}^{N_c}$ that produces deformed cloth template $\tilde{\mathcal{C}} = \{\tilde{\mathbf{c}}_i\}_{i=1}^{N_c}$ by minimizing the following energy function:

$$E^{cloth}(\tilde{\mathcal{D}}; \mathcal{C}, \mathcal{M}) = E_s^{cloth} + \lambda_r^c E_r^{cloth} + \lambda_d^c E_d^{cloth}, \quad (9)$$

where E_s^{cloth} , E_r^{cloth} , and E_d^{cloth} are the errors for shape, rigidity prior, and deformation prior, and λ_r^c and λ_d^c control their importance.

Shape E_s^{cloth} measures the distance between the vertices on $\tilde{\mathcal{C}}$ and their correspondences on \mathcal{M} :

$$E_s^{cloth}(\tilde{\mathcal{D}}; \mathcal{C}, \mathcal{M}) = \sum_{i=1}^{N_c} \|\tilde{\mathbf{c}}^i - \mathcal{M}(\tau(\mathcal{M}, \tilde{\mathbf{c}}^i))\|, \quad (10)$$

where $\tau(\cdot)$ is an index of adjacent vertex defined in Eq. (7).

Rigidity and Deformation Prior We follow two regularization terms, E_r^{cloth} and E_d^{cloth} [13] to prevent the unreasonably deformed shape. E_r^{cloth} enforces rigidity of the shape, and E_d^{cloth} encourages smoothness to the local de-

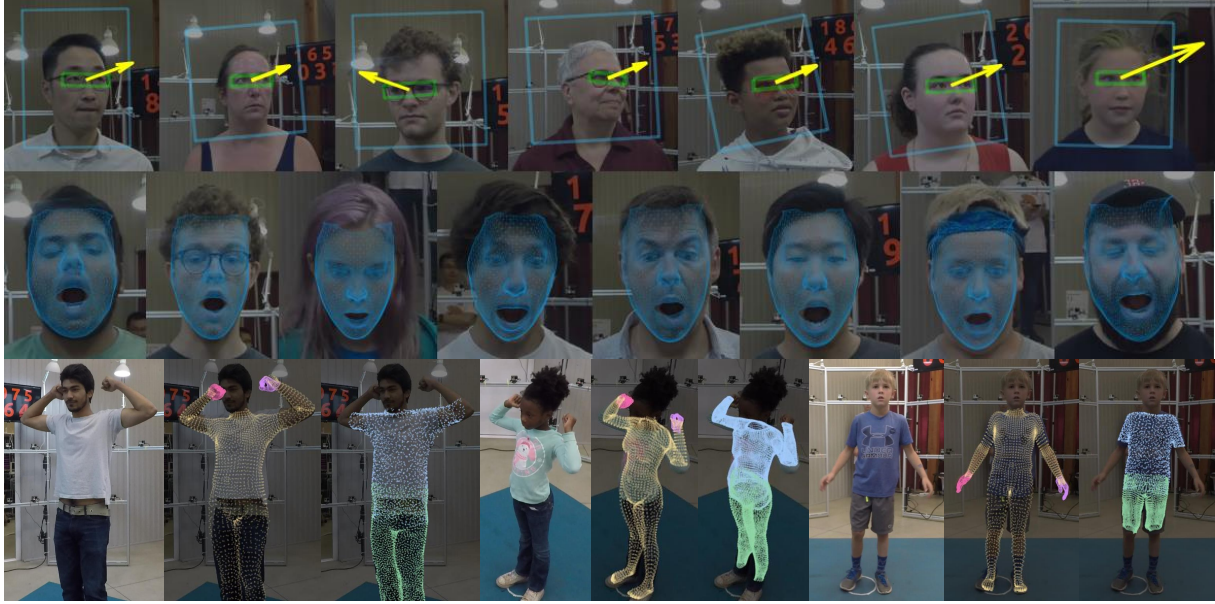


Figure 8: Additional results from diverse subjects.

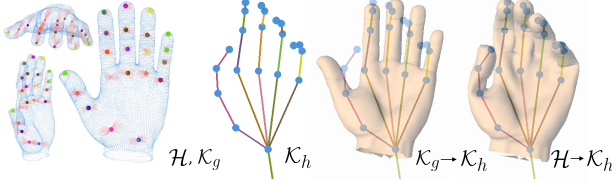


Figure 9: Hand reconstruction (Sec. 4.6). The keypoint of template hand model \mathcal{K}^g is aligned with observed key point \mathcal{K}^h . The dense hand model \mathcal{H} is deformed further to be consistent with \mathcal{K}^h .

formations:

$$E_r^{cloth}(\tilde{\mathcal{D}}) = \sum_{i=1}^{N_c} \left\| \tilde{\mathbf{R}}_i^\top \tilde{\mathbf{R}}_i - \mathbf{I} \right\|_F + \sum_{i=1}^{N_c} (\det(\tilde{\mathbf{R}}_i) - 1)^2,$$

$$E_d^{cloth}(\tilde{\mathcal{D}}; \mathcal{C}) = \sum_{i=1}^{N_c} \sum_{j \sim i} \|\Delta \tilde{\mathbf{c}}_i - \Delta \tilde{\mathbf{c}}_j\|^2, \quad (11)$$

where \mathbf{I} is the identity matrix, $\det(\cdot)$ is matrix determinant, $\|\cdot\|_F$ is Frobenius norm. $\Delta \tilde{\mathbf{c}}_i = (\tilde{\mathbf{R}}_i \tilde{\mathbf{c}}_i + \tilde{\mathbf{t}}_i) - \tilde{\mathbf{c}}_i$, $\tilde{\mathbf{c}}_j$ is the neighboring vertex of $\tilde{\mathbf{c}}_i$, and $\Delta \tilde{\mathbf{c}}_j$ is defined similar way.

After \mathcal{C} is aligned with \mathcal{M} , we align $\tilde{\mathcal{C}}$ and \mathcal{V} by minimizing the similar energy defined in Eq. (9). In this step, we further regularize alignment because direct fitting does not fully reflect the secondary motion of flexible cloth. For example, the clothes around the shoulder usually stick to the body, while the area around abdomen has more flexible movement. We thus utilize different nearest neighbor thresholds depending on cloth parts label \mathcal{L}^c . In this manner, the region with higher distance threshold is allowed to

have large deformation to correctly cover observed volume.

4.6. Hand

Hand performance is captured by fitting 3D hand template \mathcal{H} to the hands keypoint \mathcal{K}^h . For this task, we define 3D hand joints of template model \mathcal{K}^g in accordance with the order of the hand joint indices [43] where $N_h = 21$ as shown in Fig. 9. As a first step, \mathcal{K}^g is rigidly aligned with \mathcal{K}^h by minimizing the joint distance as follows:

$$\operatorname{argmin}_{s^h, \mathbf{T}^h} \sum_{i=1}^{N_h} \|s^h \mathbf{T}^h(\mathcal{K}^g(i)) - \mathcal{K}^h(i)\|^2, \quad (12)$$

where $s^h \in \mathbb{R}$ and \mathbf{T}^h denotes similarity transformation. We deform the hand model \mathcal{H} based on the local transformation field $\tilde{\mathcal{D}}^h = \{\tilde{\mathbf{R}}_i^h \in SO(3), \tilde{\mathbf{t}}_i^h \in \mathbb{R}^3\}_{i=1}^{N^g + N^h}$ by minimizing the following costs:

$$E^{hand}(\tilde{\mathcal{D}}^h; \mathcal{K}^h, \mathcal{K}^g, \mathcal{H}) = E_s^{hand} + \lambda_r^h E_r + \lambda_d^h E_d, \quad (13)$$

where the data term, $E^{hand} = \sum_i^{N_h} \|\tilde{\mathcal{D}}_i^h(\mathcal{H}(i)) - \mathcal{K}^h(i)\|$, encourages the regression of the keypoints. Here, we build the connectivity between each joint on $\mathcal{K}^g(i)$ and its neighboring vertex $\mathcal{H}(i)$ such that the joint deformation guides the entire surface deformation of \mathcal{H} in our regularization term. The regularization term, $E_r(\tilde{\mathcal{D}}^h)$ and $E_s(\tilde{\mathcal{D}}^h; \mathcal{H}, \mathcal{K}^g)$, are the same cost function defined in Eq. (11).

5. Conclusion

In this paper, we present the HUMBI dataset that captures natural human behavioral signals using a 107 multi-camera

system. As partly shown in Fig. 1, 3, 6, 8, this dataset includes 164 distinctive subjects across gender, ethnicity, age, physical condition where we provide 3D high fidelity computational models for gaze, face, finger, body, and cloth. We believe that this dataset will take us to the next level of human behavioral understanding, which will make a significant impact on millions of people’s daily lives.

References

[1] CMU Graphics Lab Motion Capture Database. <http://mocap.cs.cmu.edu/>. 2, 3, 4

[2] N. Ambady and R. Rosenthal. Thin slices of expressive behavior as predictors of interpersonal consequences: A meta-analysis. *Psychological Bulletin*, 1992. 2

[3] T. Beeler, B. Bickel, P. Beardsley, B. Sumner, and M. Gross. High-quality single-shot capture of facial geometry. *SIGGRAPH*, 2010. 2

[4] T. Beeler, B. Bickel, G. Noris, P. Beardsley, S. Marschner, R. Sumner, and M. Gross. Lightweight eye capture using a parametric model. *SIGGRAPH*, 2012. 2

[5] P. Berard, D. Bradley, M. Gross, and T. Beeler. Lightweight eye capture using a parametric model. *SIGGRAPH*, 2002. 2

[6] V. Blanz and T. Vetter. Face recognition based on fitting a 3D morphable model. *TPAMI*, 2003. 2, 3, 4, 6

[7] J. Booth, A. Roussos, A. Ponniah, D. Dunaway, and S. Zafeiriou. Large scale 3D morphable models. *IJCV*, 126(2-4):233–254, 2018. 3, 4, 6

[8] D. Bradley, T. Popa, A. Sheffer, W. Heidrich, and T. Boubekeur. Markerless garment capture. In *ToG*, volume 27, page 99. ACM, 2008. 3

[9] Z. Cao, T. Simon, S.-E. Wei, and Y. Sheikh. Realtime multi-person 2D pose estimation using part affinity fields. In *CVPR*, 2017. 5, 7

[10] D. R. Carney, A. J. C. Cuddy, and A. J. Yap. Power posing: Brief nonverbal displays affect neuroendocrine levels and risk tolerance. *Psychological Science*, 2010. 3

[11] J. R. Curhan and A. S. Pentland. Thin slices of negotiation: Predicting outcomes from conversational dynamics within the first 5 minutes. *Journal of Applied Psychology*, 2007. 3

[12] F. Devernay and O. Faugeras. Straight lines have to be straight: Automatic calibration and removal of distortion from scenes of structured environments. *Journal of Machine Vision Application*, 2001. 4

[13] M. Dou, J. Taylor, H. Fuchs, A. Fitzgibbon, and S. Izadi. 3d scanning deformable objects with a single rgbd sensor. In *CVPR*, pages 493–501, 2015. 7

[14] N. Eagle and A. S. Pentland. Reality mining: Sensing complex social systems. *Journal of Personal and Ubiquitous Computing*, 2006. 3

[15] M. A. Fischler and R. C. Bolles. Random sample consensus: A paradigm for model fitting with applications to image analysis and automated cartography. *ACM Comm.*, 1981. 5

[16] M. Gross, S. Wurmlin, M. Naef, E. Lamboray, C. Spagno, A. Kunz, E. Koller-Meier, T. Svoboda, L. V. Gool, S. Lang, K. Strehlke, A. V. Moere, and O. Staadt. Blue-c: A spatially immersive display and 3d video portal for telepresence. *SIGGRAPH*, 2003. 2

[17] R. Gross, I. Matthews, J. F. Cohn, T. Kanade, and S. Baker. Multi-PIE. *Image and Vision Computing*, 2009. 3, 4

[18] R. Gross and J. Shi. The cmu motion of body (mobo) database. *Technical Report CMU-RI-TR-01-18. Robotics Institute, Carnegie Mellon University*, 2001. 3

[19] R. Hartley and A. Zisserman. *Multiple View Geometry in Computer Vision*. Cambridge University Press, second edition, 2004. 5

[20] C. Ionescu, D. Papava, V. Olaru, and C. Sminchisescu. Human3.6M: Large scale datasets and predictive methods for 3d human sensing in natural environments. *IEEE Transactions on Pattern Analysis and Machine Intelligence*, 36(7):1325–1339, jul 2014. 2, 3, 4

[21] H. Joo, T. Simon, X. Li, H. Liu, L. Tan, L. Gui, S. Banerjee, T. S. Godisart, B. Nabbe, I. Matthews, T. Kanade, S. Nobuhara, and Y. Sheikh. Panoptic studio: A massively multiview system for social interaction capture. *TPAMI*, 2017. 2, 4

[22] M. Kazhdan and H. Hoppe. Screened poisson surface reconstruction. *ToG*, 32, 2013. 6

[23] D. Knossow, R. Ronfard, and R. Horaud. Human motion tracking with a kinematic parameterization of extremal contours. *IJCV*, 2008. 4

[24] A. Laurentini. The visual hull concept for silhouette-based image understanding. *IEEE Trans. Pattern Analysis and Machine Intelligence*, 16, 1994. 6

[25] G. Lin, A. Milan, C. Shen, and I. D. Reid. Refinenet: Multi-path refinement networks for high-resolution semantic segmentation. In *CVPR*, volume 1, page 5, 2017. 6

[26] T.-Y. Lin, M. Maire, S. Belongie, J. Hays, P. Perona, D. Ramanan, P. Dollár, and C. L. Zitnick. Microsoft coco: Common objects in context. In *ECCV*, pages 740–755. Springer, 2014. 3

[27] S. Lombardi, J. Saragih, T. Simon, and Y. Sheikh. Deep appearance models for face rendering. *SIGGRAPH*, 2018. 2

[28] M. Loper, N. Mahmood, J. Romero, G. Pons-Moll, and M. J. Black. Smpl: A skinned multi-person linear model. *ToG*, 34(6):248, 2015. 2, 3, 6

[29] K. A. F. Mora, F. Monay, and J.-M. Odobez. Eyediap: A database for the development and evaluation of gaze estimation algorithms from rgbd cameras. In *ETRA*, 2014. 3, 4

[30] O. Y. Ousley, R. Arriaga, G. D. Abowd, and M. Morrier. Rapid assessment of social-communicative abilities in infants at risk for autism. *Technical Report, Georgia Tech*, 2012. 3

[31] S. Park and J. Hodgins. Capturing and animating skin deformation in human motion. *SIGGRAPH*, 2006. 3, 4

[32] P. Paysan, R. Knothe, B. Amberg, S. Romdhani, and T. Vetter. A 3D face model for pose and illumination invariant face recognition. *AVSS*, 2009. 3, 4

[33] A. S. Pentland. Social dynamics: Signals and behavior. In *International Conference on Developmental Learning*, 2004. 3

[34] A. S. Pentland. Socially aware computation and communication. *IEEE Computer*, 2005. 3

[35] A. S. Pentland. Honest signals: How they shape our world. *IEEE Signal Processing Magazine*, 2008. 3

[36] G. Pons-Moll, S. Pujades, S. Hu, and M. J. Black. Clothcap: Seamless 4d clothing capture and retargeting. *ToG*, 36(4):73, 2017. 3, 4, 7

[37] G. Pons-Moll, J. Romero, N. Mahmood, and M. J. Black. Dyna: A model of dynamic human shape in motion. *SIGGRAPH*, 2015. 2, 3, 4

[38] J. M. Rehg, G. D. Abowd, A. Rozga, M. Romero, M. A. Clements, S. Sclaroff, I. Essa, O. Y. Ousley, Y. Li, C. Kim, H. Rao, J. C. Kim, L. L. Presti, J. Zhang, D. Lantsman, J. Bidwell, and Z. Ye. Decoding children’s social behavior. In *CVPR*, 2013. 3

[39] S. Rusinkiewicz and M. Levoy. Efficient variants of the icp algorithm. In *Third International Conference on 3-D Digital Imaging and Modeling*, 2001. 7

[40] J. L. Schönberger and J.-M. Frahm. Structure-from-motion revisited. In *CVPR*, 2016. 4, 6

[41] L. Sigal, A. O. Balan, and M. J. Black. HumanEva: Synchronized video and motion capture dataset and baseline algorithm for evaluation of articulated human motion. *IJCV*, 87(1-2):4, 2010. 2, 3, 4

[42] T. Sim, S. Baker, and M. Bsat. The CMU pose, illumination, and expression (PIE) database of human faces. In *Tech. Report, CMU-RI-TR-01-02, Robotics Institute, Carnegie Mellon University*, 2001. 3

[43] T. Simon, H. Joo, I. A. Matthews, and Y. Sheikh. Hand key-point detection in single images using multiview bootstrapping. In *CVPR*, volume 1, page 2, 2017. 3, 4, 8

[44] B. Smith, Q. Yin, S. Feiner, and S. Nayar. Gaze locking: Passive eye contact detection for humanobject interaction. In *UIST*, 2013. 4

[45] Y. Sugano, Y. Matsushita, and Y. Sato. Learning-bysynthesis for appearance-based 3d gaze estimation. In *CVPR*, 2014. 3, 4

[46] X. Sun, Y. Wei, S. Liang, X. Tang, and J. Sun. Cascaded hand pose regression. In *CVPR*, 2015. 3

[47] J. S. Supancic, G. Rogez, Y. Yang, J. Shotton, and D. Ramanan. Depth-based hand pose estimation: data, methods, and challenges. In *ICCV*, 2015. 3

[48] D. Tang, H. J. Chang, A. Tejani, and T.-K. Kim. Latent regression forest: Structured estimation of 3d articulated hand posture. In *CVPR*, 2014. 3

[49] J. Tompson, M. Stein, Y. Lecun, and K. Perlin. Real-time continuous pose recovery of human hands using convolutional networks. *TOG*, 2014. 3, 4

[50] A. Vinciarelli, M. Pantic, and H. Bourlard. Social signal processing: Survey of an emerging domain. *Image and Vision Computing*, 2009. 2, 3

[51] A. Wetzler, R. Slossberg, and R. Kimmel. Rule of thumb: Deep derotation for improved fingertip detection. In *BMVC*, 2016. 3, 4

[52] R. White, K. Crane, and D. A. Forsyth. Capturing and animating occluded cloth. In *ToG*, volume 26, page 34. ACM, 2007. 3

[53] B. Wilburn, N. Joshi, V. Vaish, E.-V. Talvala, E. Antunez, A. Barth, A. Adams, M. Levoy, and M. Horowitz. High performance imaging using large camera arrays. *SIGGRAPH*, 2005. 2

[54] J. S. Yoon, Z. Li, and H. S. Park. 3d semantic trajectory reconstruction from 3d pixel continuum. *CVPR*, 2018. 2, 6

[55] S. Yuan, Q. Ye, B. Stenger, S. Jain, and T.-K. Kim. Big hand 2.2m benchmark: Hand pose data set and state of the art analysis. In *CVPR*, 2017. 3, 4

[56] X. Zhang, Y. Sugano, M. Fritz, and A. Bulling. Appearance-based gaze estimation in the wild. In *CVPR*, 2015. 3, 4